Article

Photocatalytic Uphill Reactions with Apparent Quantum Efficiency over 10%

Liang Tian, Alberto García-Baldoví * and Hermenegildo García *

Instituto de Tecnología Química, Universitat Politècnica de València-Consejo Superior de Investigaciones Científicas, Universitat Politècnica de València, Av. de los Naranjos s/n, 46022 Valencia, Spain

* Correspondence: algarbal@itq.upv.es (A.G.-B.); hgarcia@qim.upv.es (H.G.)

Abstract: Despite the massive research effort in photocatalysis for solar fuels production, the efficiencies reached are still much lower than required for practical application. The present work proposes that to reach high apparent quantum yields in photocatalytic solar-to-chemicals conversions, mechanistically simple reactions should be used. Thus, instead of H_2 generation or photocatalytic CO_2 reduction, the present work reports data on the photocatalytic conversion of redox mediators that upon a single electron transfer convert the most stable form of a reversible redox pair into the highest energy species of the redox coupling. Specifically, by using two metal-organic frameworks as photocatalysts, the reduction of three bipyridinium dications and the oxidation of ferrocyanide and NADH was studied. Very high apparent quantum efficiencies were measured in most of the cases, the apparent quantum yields being particularly high for the conversion of methyl viologen to the corresponding radical cation and the photooxidation of ferrocyanide to ferricyanide. These findings outline a new strategy for solar energy conversion that emphasizes efficiency and mechanistic simplicity, shifting the focus from complex multi-step transformations such as water splitting or CO_2 reduction to more straightforward reactions capable of storing highly efficiently sunlight in high-energy chemical states.

Keywords: photocatalysis; apparent quantum yield; redox mediators

1. Introduction

Photocatalysis with solar light is widely regarded as a sustainable strategy to produce renewable fuels [1–3]. Among possible solar fuels, hydrogen evolution [4–7], CO_2 conversion [8,9], H_2O_2 generation [10], and nitrogen reduction [11] have attracted considerable attention. Over the past decades, extensive research has advanced our understanding of the photocatalytic mechanisms, introduced advanced photophysical techniques, and led to the evaluation of numerous photocatalysts [4,8,12–14]. Yet, despite this massive effort, photocatalytic efficiencies remain far from practical requirements and most materials exhibit solar-to-chemical conversion efficiencies below 5%, well under the threshold for economic viability [15,16]. Attempts at rational photocatalyst design, semiconductor coupling, or addition of co-catalysts—among other strategies—have yielded only modest improvements, leaving cost-effectiveness and efficiency as major challenges.

This situation stands in sharp contrast to photovoltaics, where commercial solar cells routinely achieve efficiencies above 20% [17–19]. Both technologies share key steps—light absorption, electron excitation across the band gap, charge separation, and carrier migration—differing mainly in whether photogenerated electrons are harvested by an external circuit or consumed in surface chemical reactions [20]. The performance gap between solar photovoltaics and photocatalysis is striking. For instance, overall water splitting for hydrogen production

typically achieves less than 1% solar-to-chemical efficiency [6], often near 0.1% [21], leading some to argue whether photocatalytic water splitting [22] and CO_2 reduction [23] could ever be feasible.

Meanwhile, molecular photochemistry demonstrates that highly efficient light promoted reactions are possible. Many reactions involving organic photosensitizers exceed 10% efficiency, and some approach unity, such as singlet oxygen generation to name a widely studied photochemical process [24,25]. These cases suggest that a fresh perspective is needed in solar photocatalysis, shifting the focus from difficult target products to simpler, high-efficiency light-to-chemical reactions that, however, can yield stable energy carriers. Low efficiency in current systems is most frequently linked to intrinsic photocatalyst properties, such as weak light absorption, fast electron/hole recombination, and interfacial charge transfer resistance. It is a main concept of the present study that the main bottleneck of current poor photocatalytic efficiencies for solar fuels production should be put on the reaction products and the slow kinetics of multi-step reactions involving consecutive steps of coupled electron–proton transfer [26]. Designing processes with much simpler mechanisms can result in much higher solar-to-chemical energy conversion efficiencies that could open new opportunities for solar energy storage.

In the present work such an approach has been adopted by targeting the photocatalytic generation of water-stable reduced or oxidized species formed in a single step by straightforward single-electron or single-hole transfer. These thermodynamically uphill products formed by single electron transfer serve as redox mediators capable of storing solar energy that can later be released on-demand chemically or electrochemically, for example in a battery configuration. By carefully selecting redox pairs with potential matched to the conduction and valence band energy edges of the photocatalyst, it is shown that photon-to-chemical conversion efficiencies above 10% are achievable. Moreover, the stored energy can be used for hydrogen evolution on demand. Thus our results offer a path toward practical implementation.

2. Results and Discussion

The present study requires the careful selection of photocatalysts, probe molecules, and irradiation conditions to test the central hypothesis, i.e., that photocatalysts that perform poorly in overall water splitting or CO_2 reduction may nonetheless be much more effective for alternative photocatalytic transformations capable of storing solar energy in chemical compounds. The following sections describe the photocatalysts, molecular probes, and reaction conditions employed in this work.

2.1. Photocatalysts

Our strategy for solar energy conversion and storage in redox mediator pairs began with the selection of two representative photocatalysts and the determination of their optoelectronic properties, including band gap, conduction and valence band positions, and charge-transfer resistance to the electrolyte. While the band-related parameters govern the thermodynamic driving force of the reactions, charge-transfer resistance provides insight into the kinetics. In this case, the latter is particularly critical, as the process ideally involves a single electron transfer between the excited transient charge separated state of the photocatalyst and the redox mediator. Building on our previous experience with metal–organic frameworks (MOFs) as photocatalysts [12], we selected two robust and well-studied materials: UiO-66-NH$_2$ and MIL-125-NH$_2$. Both MOFs contain aminoterephthalate linkers coordinated either to $Zr_6(OH)_4O_4^{12+}$ clusters in UiO-66(Zr)-NH$_2$ or to $Ti_8O_8(OH)_4^{12+}$ clusters in MIL-125(Ti)-NH$_2$. These frameworks were synthesized following established procedures, using aminoterephthalic acid as the organic linker, acetic acid as modulator and $ZrCl_4$ or $Ti(OiPr)_4$ as the metal precursors [27,28]. The X-ray diffraction patterns, analytical compositions and spectroscopic data obtained for both MOFs were consistent with reported values, confirming their phase purity and structural integrity. Figure 1 illustrates the crystal structures of UiO-66-NH$_2$ and MIL-125-NH$_2$, highlighting their open porosity.
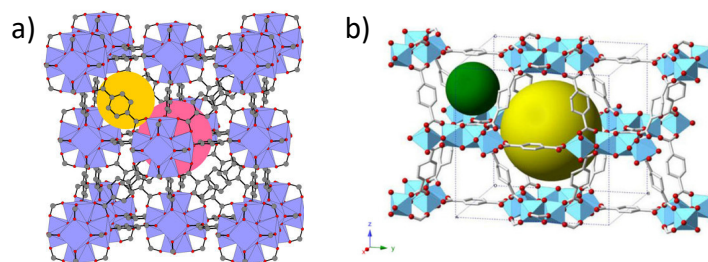

Figure 1. Structure of UiO-66(Zr) (**a**) and MIL-125(Ti) (**b**) showing the metal nodes and terephthalate linkers. The two voids in each structure, either tetrahedral (orange and green) and octahedral (red and yellow) have been highlighted. Taken from open access Refs. [25,29].

Optoelectronic properties of UiO-66(Zr)-NH$_2$ and MIL-125(Ti)-NH$_2$ were characterized using appropriate tools. The –NH$_2$ substituent in the terephthalate ring introduces a $n \rightarrow \pi^*$ electronic transition that is responsible for the appearance of an absorption band in the visible region of the optical spectrum with absorption maximum at about 360 nm and extending into the visible with onset at 450 nm. The bandgap was estimated by the Tauc plot of the diffuse reflectance UV-Vis absorption spectra of these two MOFs considering them as indirect semiconductors [13,30]. Figure S1 in supporting information presents the diffuse reflectance spectra for the series of photocatalyst as well as the corresponding Tauc plots. The energy of the valence bands was determined from the energy of the onset of current intensity of emitted photoelectrons in XPS measurements upon correction of the work function of the instrument, as illustrated in Figure S2. Conduction band potentials were estimated by the Mott-Schottky plot from electrochemical impedance spectroscopy data. Figure S3 present these measurements. Experimental section provides details of the instruments and procedures used to determine these band energies, while Figure 2 presents the band alignment for UiO-66(Zr)NH$_2$ and MIL-125-NH$_2$ calculated in the present work for the samples under study. These values were in relatively good agreement with data previously reported in the literature for these materials with a maximum deviation of 0.2 eV [31,32].
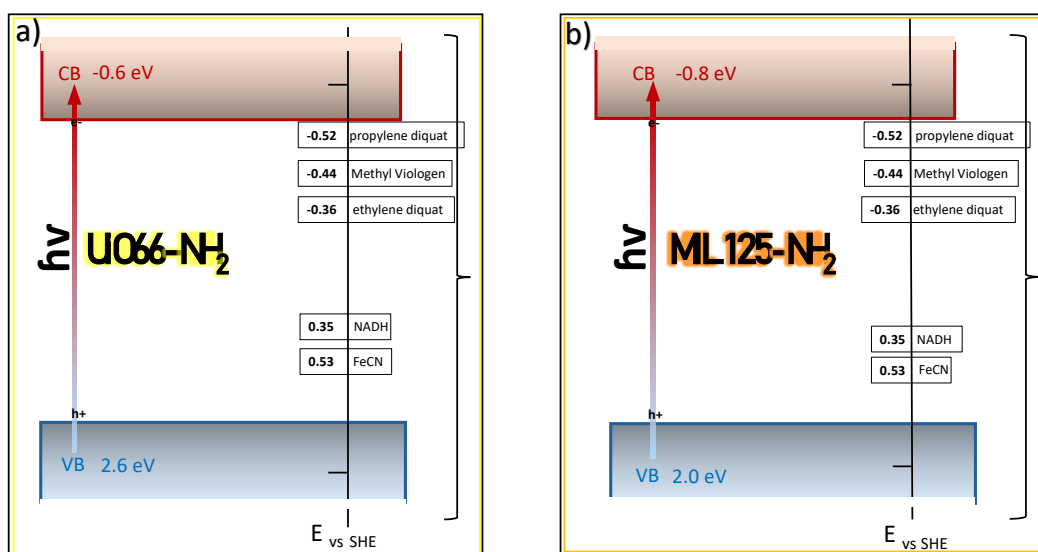

Figure 2. Energy diagram for (**a**) UiO-66(Zr)-NH$_2$ and (**b**) MIL-125(Ti)-NH$_2$ in comparison to the standard redox potentials of the mediators under study.

Both UiO-66(Zr)-NH$_2$ and MIL-125-NH$_2$ have been widely used in the literature for overall water splitting and photocatalytic CO$_2$ reduction, where they exhibit unsatisfactory efficiency far from the minimum requirements for application [9,12,33,34].
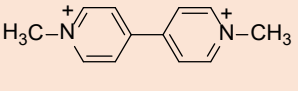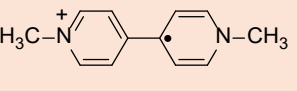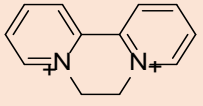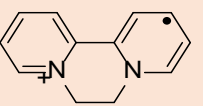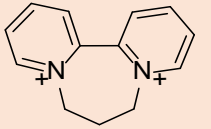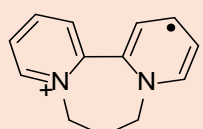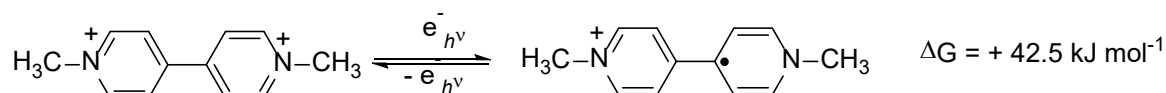
2.2. Redox Mediators

In the present case to prove the hypothesis that these two photocatalysts can exhibit considerably higher efficiency for simpler reactions five redox pair mediators differing in their redox potential were selected. Table 1 presents their structures and their redox potential. Their selection was based on the known electrochemical behaviour of these compounds [35–37]. particularly reaction simplicity and the reversibility of the redox process. Reversibility should allow to store the highest energy form of the redox pair for long periods in aqueous media until needed.

The list includes three bipyridinium dications as electron mediators that will become reduced in the photocatalytic process by a single electron transfer. Importantly, the electrochemical process is reversible and the reduced form of these bipyridiniums are stable radical cations that can be easily monitored by their characteristic optical absorption spectrum that exhibit vibrational fine structure [38]. In fact, the strong visible light absorption of bipyridinium radical cations is responsible for their characteristic blue-green color that combined with their stability in the absence of oxygen is responsible for the visual detection of their generation. Development of blue color upon irradiation of deaerated suspensions of MOFs in the presence of bipyridiniums has been taken as a compelling evidence of the occurrence of photoinduced charge separation in the process [39–41]. This absorption band can also be used to determine quantitatively the concentration of bipyridinium radical cation. One additional property of these bipyridiniums is that the redox process is pH independent [42]. The three selected bipyridinium

dications are methyl viologen and two cyclic 2,2′-bipyridiniums screening a range of redox potential from −0.36 to −0.52 V vs. RHE. In that way, the reduced bipyridinium radical cations can store photochemical energy by converting the most stable oxidized form into the corresponding reduced form having higher chemical energy but still being indefinitely persistent in aqueous medium in the absence of oxygen. Scheme 1 illustrates the concept and the process.

Table 1. Redox mediators used in the present study with indication of their standard redox potentials. Light orange highlights those three mediators used in the oxidized form to become reduced (electron mediators), while light green shows the two mediators used in the reduced form to be oxidized by holes (oxidation mediators).

Mediator	E° (V vs. SHE)	ΔG (kJ mol⁻¹)
H_3C-N^+=⟨⟩-⟨⟩=N^+-CH_3 / H_3C-N^+=⟨⟩-⟨⟩•$N-CH_3$	−0.44	42.5
(bipyridinium) / (bipyridinium radical)	−0.36	34.7
(bipyridinium) / (bipyridinium radical)	−0.52	50.2
$Fe(CN)_6^{3-}$ / $Fe(CN)_6^{4-}$	0.47	45.3
$NAD^+ + H_+ + 2e_{h\nu}$ / NADH	0.35	67.6

$$H_3C-N^+{=}⟨⟩{-}⟨⟩{=}N^+{-}CH_3 \underset{-\,e^-_{h\nu}}{\overset{e^-_{h\nu}}{\rightleftharpoons}} H_3C-N^+{=}⟨⟩{-}⟨⟩{\bullet}N{-}CH_3 \qquad \Delta G = +\,42.5\ \text{kJ mol}^{-1}$$

- simple reaction mechanism involving only an electron
- both species of the redox pair are stable in H_2O
- process monitored by optical absortion spectroscopy
- facile quantification
- ΔG as large as possible by matching the conduction band energy

Scheme 1. Illustration of the concept of the present study. $e^-_{h\nu}$ refers to photogenerated electrons.

As it is indicated in this Scheme 1 and to achieve a high energy conversion efficiency, the redox potential of the reduction mediator should be as close as possible to the conduction band reduction potential of the photocatalyst. Figure 2 shows the relative energy of the conduction and valence band energy values for UiO-66(Zr)-NH_2 and MIL-125(Ti)-NH_2 and the position of the standard potential of the redox mediators. A certain overpotential should probably be required to ensure that the photocatalytic reaction occurs at high reaction rate. After the photocatalytic reaction and the formation of the mediator species in their highest energy form, the chemical energy could be released on demand to promote a chemical reaction or to release electrical energy at will.

Continuing with the concept of the present paper, two redox mediators reacting with holes were also selected. The first one is ferrocyanide that is a common standard in electrochemistry with a fully reversible oxidation peak to ferricyanide [43]. Also in this case, the photocatalytic process and the concentration of ferricyanide can be easily determined by colorimetry following the change in the colour from the pale-yellow characteristic of ferrocyanide to the orange-red corresponding to ferricyanide with absorption maximum at about 430 nm [44]. The second oxidation mediator is nicotinamide adenine dinucleotide (NADH), a biomolecule involved in the energy metabolism as reducing agent. In this case, the reaction involves coupled electron and proton transfer, thus making the redox process alike to the elementary steps that occur in photocatalytic CO_2 reduction, with the notable difference that in the case of NADH/NAD^+ redox piair there is a single H^+ released [45]. In addition, the use of this biomolecule could open the field of the present study not only to energy storage chemicals, but also to photocatalysis for relevant biochemical processes. In the case of NADH, the course of the oxidation can be
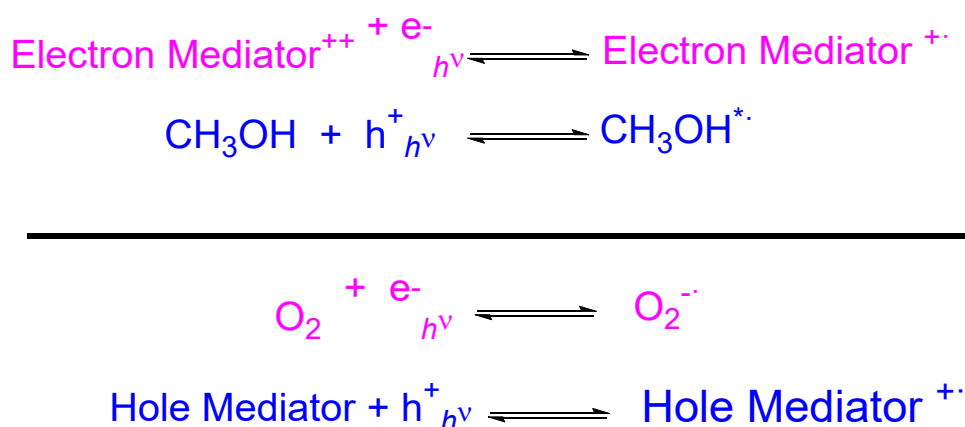
followed monitoring the disappearance of its characteristic 340 nm band. The redox potentials of ferrocyanide and NADH are also indicated in Table 1.

For these five redox mediators there is abundant data in the literature showing the reversible redox cycling and the corresponding potentials. Table 1 shows the structure for the mediators employed in the present study and their reduction potential measured by us in aqueous solution at 1 mM concentration using 0.1 M Na_2SO_4 as electrolyte. Overall, the experimental values measured by us are in particularly good agreement with those reported in the literature, once the different experimental conditions are taken into consideration.

2.3. Irradiation Conditions

By studying the performance of UiO-66(Zr)-NH_2 and MIL-125(Ti)-NH_2 as photocatalysts for these simple redox mediators, the objective is to determine the apparent quantum efficiency in these reactions, trying to correlate the energy of the conduction and valence bands with the redox potential of the mediators and the apparent light-to-chemical energy conversion efficiency of the process. The term apparent refers that we are considering all the photons emitted by the light source in the calculations of the quantum yield, even though a fraction of these photons will be transmitted throughout the cuvette or scattered by the colloidal suspension, without being absorbed. In other words, the ratio between emitted and absorbed photons was considered as 1. The reactions were carried out under magnetic stirring in quartz cuvettes, allowing in this way to follow the course of the reaction by optical absorption spectroscopy. Under the conditions used in the present study using probe concentrations in the range of 0.1 mM, and with the output of a white LED, some of the reactions were complete in less than 1 min. Thus, apparent quantum yield values are referred to 10 s irradiation.

It has to be noted that in all photocatalytic reactions, the consumption rate of photogenerated e^- and h^+ must match. Therefore, the experiments with electron acceptor bipyridinium dications irradiations (light orange shadow highlight in Table 1) were carried out in H_2O containing 20 wt.% of CH_3OH as sacrificial electron donor. Analogously, in the case of the photocatalytic oxidation of electron donor probes the process was carried out in O_2-saturated aqueous solutions to manage electron consumption. Scheme 2 shows the complete photocatalytic reaction taking place with the two types of redox mediators under study.
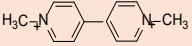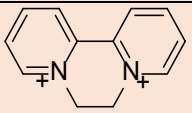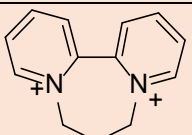
$$\text{Electron Mediator}^{++} + e^-_{h\nu} \rightleftharpoons \text{Electron Mediator}^{+\cdot}$$

$$CH_3OH + h^+_{h\nu} \rightleftharpoons CH_3OH^{*\cdot}$$

$$O_2 + e^-_{h\nu} \rightleftharpoons O_2^{-\cdot}$$

$$\text{Hole Mediator} + h^+_{h\nu} \rightleftharpoons \text{Hole Mediator}^{+\cdot}$$

Scheme 2. Complete photocatalytic reactions taking place when using the electron or hole redox mediators indicated in Table 1. Pink and blue colour refers to the reduction and oxidation semi reactions, respectively. The *hv* subscript corresponds to photogenerated transient charge carriers, either electrons in the conduction band or holes in the valence band.

By having a look to the complete chemical equations shown in Scheme 2, it should be commented that the present study assumes that apparent quantum yields of redox mediator conversion should be close to the maximum possible value. This assumption requires that the photocatalytic oxidation of CH_3OH—in the case of bipyridiniums—and photocatalytic reduction of O_2—in the case of the oxidation redox mediators—are much faster than the semi reaction of the probes. However, considering the simplicity of the chemical processes undergone by the redox mediator this assumption may not be totally correct, and the rate of the two semi reactions could be comparable. If this were the case, the maximum quantum yield of the photocatalytic conversion of the mediator semi reaction could be even higher than the values estimated in the present process.

As expected, irradiation of a suspension of the photocatalysts in the presence of the redox mediators as probes leads to visual coloration changes that are reflected in variations in the optical absorption spectra in accordance with the formation of the corresponding radical cation by a single electron reduction in the case of bipyridiniums

or one single electron oxidation in the case of ferrocyanide. Although, in the case of NADH, oxidation cannot be visually observed, optical spectra in the near UV range also showed the expected disappearance of the characteristic NADH absorption band at λ_{max} 340 nm Figure S4. These spectral changes allowed us to determine the concentration of the probes and, therefore, to determine the apparent quantum efficiency of the process. Equation (5) in the experimental section was used to determine these efficiency values that are presented in Table 2. In most of the cases the complete photocatalytic conversion of the probe took place in less than one minute.

Table 2. Apparent quantum efficiency values and solar-to-chemical energy conversion for the five redox mediators under consideration using UiO-66(Zr)-NH$_2$ and MIL-125(Ti)-NH$_2$ as photocatalysts. Data correspond to the average of three independent measurements.

	UiO-66(Zr)-NH$_2$		MIL-125(Ti)-NH$_2$	
	Apparent Quantum Yield (%)	Light-to-Chemical Energy Conversion Efficiency	Apparent Quantum Yield (%)	Light-to-Chemical Energy Conversion Efficiency
H$_3$C-N⁺=⟨ ⟩-⟨ ⟩=N⁺-CH$_3$ (methyl viologen)	>90	20 ± 4	88 ± 5	19 ± 4
2,2′-bipyridinium dication	<1	<1	2 ± 2	2 ± 2
tricyclic 2,2′-bipyridinium	1±1	1±1	-- [a]	-- [a]
$Fe(CN)_6^{4-}$	67 ± 5	12 ± 3	64 ± 5	11 ± 3
NADH	30 ± 5	8 ± 2	-- [a]	-- [a]

[a] Too low to be determined with some accuracy.

From the apparent quantum yield values shown in Table 2 the first important comment is that these yields are obviously considerably much higher than those that have been achieved so far in hydrogen evolution or overall water splitting. Thus, these results support the concept of the present study that intrinsically low efficiencies derive in some extent from the complex mechanism of the photocatalytic reaction. These complex mechanisms over burden other limitation factors inherent the photocatalysts. An additional point refers to the influence of the mass transport and diffusion of the mediators through the MOF microporous system on the apparent quantum yield. Reported pore size values for UiO-66(Zr)-NH$_2$ vary from 0.8 to 1.1 nm, while MIL-125(Ti)-NH$_2$ has tetrahedral and octahedral cages accessible through windows of 0.5 and 0.7 nm, approximately. Since the mediators being considered in Table 1 are ions, their diffusion within the MOF micropores should be accompanied also by that of charge compensating ions to ensure electroneutrality of the system [46]. This may decrease the diffusion coefficient of the present mediators in comparison to others alternative corresponding to neutral molecules, Thus, it could be that the quantum yield for other mediators having faster diffusion constants could be even higher than those measured in the present study. Both MOFs perform similarly as photocatalysts. The highest apparent quantum efficiency values were reached for the reduction of methyl viologen by UiO-66(Zr)-NH$_2$, somewhat higher than the value measured for MIL-125(Ti)-NH$_2$. That is also very high. It is interesting to note that in comparison to the apparent quantum yield values reached for methyl viologen, the other two 2,2′-bipyridinium dications reached much lower apparent quantum yields. Although further studies are necessary to determine the reasons for this contrasting behavior, it is proposed that diffusion inside the pores of the MOFs is much easier for methyl viologen due to its smaller kinetic diameter than for the tricyclic 2,2′-bipyridiniums that should have much smaller diffusion coefficients, this limiting the access to internal photogenerated electrons. Also, remarkably high apparent quantum efficiency value has been measured for the oxidation of ferrocyanide using UiO-66(Zr)-NH$_2$. Worth noting is also the apparent quantum yield measured for NADH oxidation, in spite that its large molecular size impedes this mediator to access the MOF pore system and it can only become oxidized at the external surface of the crystals. Probably for this reason, the apparent quantum yield for NADH oxidation in MIL-125(Ti)-NH$_2$ is very low and photooxidation of this mediator was observed only in the case of UiO-66(Zr)-NH$_2$. photocatalyst. It should be noted that although diffusion seems to control AQY values, there are many other factors, like the energy of the frontier orbitals, redox potentials and the rate of electron transfer that should also influence the efficiency of the process. Overall, the present results support the concept of the present study, suggesting that simple photocatalytic transformations result in much higher apparent quantum yields that those achieved so far in photocatalytic solar fuels production.

Regarding visible light-to-chemical efficiency the relative energy of the light used in the process and the energy of the redox species formed must be considered as indicated in Equation (4) of the experimental section. In simple terms, even though most of the photons can promote the reduction of methyl viologen to the corresponding radical cation, the relative energy of this oxidized form is low in comparison to that of the photons used in the process. This results in a lower light-to-chemical energy conversion that however is still remarkable and comparable to efficiencies achieved so far in photovoltaics. The fact that the other two bipyridinium dications exhibit much lower apparent quantum yields does not allow to have a more detailed information about how the alignment of the conduction band minimum energy of the photocatalyst affects the light-to-photon energy conversion.

Light conversion efficiency of the photocatalytic reactions under the present favorable conditions was estimated by dividing ΔG of the chemical process taking place in the mediator by the visible light energy consumed in this change. Increment of the chemical energy ΔG is related to the redox potential of the process. Equation (4) in the experimental section corresponds to the formula used to determine light-to-chemical energy conversion. It is pertinent to comment that these simple calculations refer exclusively to the energy stored in the redox mediator. However, as indicated in Scheme 2, the process also consumes in the present case either CH_3OH or O_2 as hole or electron quencher, respectively. To this respect it has to be commented that in the case of photocatalytic H_2 evolution, CH_3OH has also been commonly used as hole scavenger. Even using CH_3OH the quantum efficiency for photocatalytic hydrogen generation is still low. This contrasts with the results obtained in the present case. In the case of the two oxidation mediators, O_2 is consumed in the process as sacrificial electron quencher (Scheme 2).

To put the values presented in Table 2 in a broader context, Table S1 in the supporting information provides some apparent quantum yields and light conversion efficiency data reported in the literature. As it can be seen there, the results achieved for methyl viologen as electron mediator and ferrocyanide as hole mediators are among the highest efficiency values achieved so far. Even the efficiency achieved for a bulk molecule like NADH is quite remarkable and comparable to the best values found in the literature. Worth noting is that in the present case, the photocatalytic systems does not contain noble metals or other co-catalyst and the photocatalyst is constituted by a single component and not by a heterojunction. It is known that co-catalysts can increase the efficiency of photocatalysts and that the combination of two photocatalysts with appropriate staggered band alignment can form S-heterojunctions with increased charge separation efficiency in comparison to a single photocatalyst. Nevertheless that in the present case there is still room for further improvement, the present results show that the present strategy based on one electron transfer can work quite well to develop highly efficient photocatalytic processes for light energy storage.

From the above discussion it appears that MOFs as photocatalysts can generate the most energetic form in a redox pair starting from the most stable species of the pair. As indicated in Table 2, this can serve to store chemical energy. In the absence of oxygen, bipyridinium mediators have been reported to be stable in water for extended periods [47]. However, the chemical potential of the most energetic form of the pair can be released under certain circumstances and conditions. Thus, it has been reported that the addition of colloidal platinum to methyl viologen radical cation promotes reoxidation of this species to the most stable methyl viologen form, evolving equivalent amounts of H_2 [48,49]. Also in our hands, the blue reduced form of methyl viologen becomes decolorized upon addition of colloidal Pt nanoparticles with the visual evolution of bubbles that can be attributable to H_2 according to the literature.

Considering the equations of Scheme 2 as corresponding to photochemical processes, an initial estimation of the ΔG energy of these processes can be estimated by applying $\Delta G = -n F \Delta E$, in which ΔG indicates the Gibbs energy change, n is the number of electrons involved in the process, and ΔE is the redox potential difference between the mediator and the CH_3OH or O_2 as sacrificial agents. Based on the above equation and considering the $E^o{}_{red}$ values given in Table 1 for the mediators and the values of $+2.2$ V and -0.33 V for $CH_3OH^{\cdot-}/CH_3OH$ and $O_2/O_2^{\cdot-}$ pairs respectively, ΔG can be estimated. In the case of the photocatalytic reduction of methyl viologen, $\Delta G = -1 \times 96,500 \times (-2.64) = 254.76$ kJ mol^{-1}, and for ferrocyanide oxidation $\Delta G = -1 \times 96,500 \times (-0.8) = 77.2$ kJ mol^{-1}. Obviously, these simple calculations have to be refined by an accurate determination of the reaction products and the processes derived from the reactive intermediates formed from the sacrificial agents.

Furthermore, considering that previous photocatalytic reactions can form a reduced (case of electron mediators) and an oxidized (case of hole mediators) species, the possibility to recover the energy as a battery by combining two different mediators was considered. To proof this possibility two independent experiments were carried out using UiO-66(Zr)-NH$_2$ as photocatalyst in which the two most efficient semi reactions according to Table 2 to generate the radical cation from the methyl viologen on one hand and ferricyanide from ferrocyanide on the other were carried out. Then, the resulting solutions used as anode and cathode of a battery, respectively. The resulting open circuit voltage measured for this device was 0.38 V, while a small light bulb was powered with this system. We noticed that the open circuit voltage of the battery was much lower than the theoretical 0.91 V standard potential for a battery

having methyl viologen radical cation//ferricyanide as anode//cathode, respectively. Possible reasons for this lower voltage include large internal cell resistance due to unoptimized configuration and large distance between electrodes, the presence of methanol in the methyl viologen radical cation anode, residual O_2 in ferricyanide solution and the low concentration of active species. In any case these preliminary results show that upon additional improvement, the system reported here can serve to store solar energy in the form of chemical potential.

Charge transfer resistance measured for UiO-66-(Zr)-NH$_2$ on glassy carbon electrodes using 0.1 M Na$_2$SO$_4$ as electrolyte determined from the Nyquist plot gave a value of about 7 kW, meaning that the process of single electron transfer still has a considerable resistance and the efficiency of the photocatalytic redox mediators could be further improved by diminishing the charge transfer. It is worth commenting that similar values of charge transfer resistance for these MOFs have been reported in the literature [50] and that it appears that this parameter is highly sensitive to the medium and measure conditions.

3. Conclusions

The present work proposes a novel approach to photocatalysis for solar-to-chemicals energy storage in which, instead to focus on the obtainment of conventional fuels, like H_2 or CO_2 reduction products, the emphasis is put in carrying out the simplest possible photocatalytic processes in order to reach high efficiency in terms of high apparent quantum yields. In that way, the threshold to develop an economically viable photocatalytic process can be more easily reached. We have found that very high apparent quantum yields can be obtained for two MOFs as photocatalysts, but it is suggested that this strategy could also work equally well for other photocatalysts, particularly metal oxides and graphitic carbon nitrides. Despite the high apparent quantum yield that have been reached, the energy balance of the process still requires much attention to align better the frontier band energy of the photocatalysts with the redox potential of the redox mediators. In addition, the fact that the complete chemical reaction involves the use of sacrificial agents has to be properly considered. Nevertheless, although much work is still needed to fully develop the here proposed strategy, the present results open an avenue to further optimize simplest one-electron photochemical process coupled with convenient semi reactions.

4. Experimental Section

4.1. Chemicals

Methyl viologen dichloride, potassium ferrocyanide, NADH, 2,2′-bipyridine, 1,2-dibromoethane 1,3-dibromopropane, 2-aminoterephthalic acid, acetic acid, DMF and other chemicals were purchased from Sigma Aldrich and used as received. Solvents were dried using an automated solvent drier. Photocatalytic reactions were carried out in deionized Milli-Q water.

4.2. Preparation of Materials

4.2.1. Preparation of UiO-66(Zr)-NH$_2$

UiO-66(Zr)-NH$_2$ was prepared according to the literature [51]. In brief, 233 mg ZrCl$_4$ were dissolved in 20 mL DMF having 2 mL acetic acid. Then 181 mg 2-aminoterephthalic acid and 0.3 mL of H$_2$O were added under stirring. The mixture was transferred to a Teflon-lined autoclave and heated at 120 °C for 18 h. After this time, the suspension was cooled and the pale-yellow crystals of UiO-66(Zr)-NH$_2$ were collected by filtration. The solid was washed first with DMF and then repeatedly with ethanol to remove residual solvent and modulator. The soaked crystals well stirred overnight in fresh alcohol and finally dried in a diseccator to give UiO-66(Zr)-NH$_2$ as a yellow powder.

4.2.2. Preparation of MIL-125(Ti)NH$_2$

MIL-125(Ti)-NH$_2$ was prepared following the reported procedure [52]. A 40 mL screw-cap vial was charged with 15 mL of DMF (15 mL) and 5 mL of ethanol (5 mL). Then, 181 mg of 2-aminoterephthalic acid was dissolved by heating under magnetic stirring. After complete dissolution, 1 mL of glacial acetic acid was added to the synthesis mixture as modulator together with 0.20 mL of water to promote hydrolysis of Ti precursor. Afterwards, 0.50 mL of titanium isopropoxide was added dropwise under vigorous stirring. The mixture turned yellow and slightly opalescent. Then, the vial was capped tightly and heated at 150 °C for 18 h. After this time, the mixture was cooled and the solid formed collected by filtration, washed once with 10 mL of DMF (15 mL) and three times with 20 mL aliquots of methanol. The yellow powder of MIL-125(Ti)-NH$_2$ was left overnight in fresh methanol overnight and stored in a desiccator.

4.2.3. Synthesis of 1,1′-ethylenediyl-2,2′-bipyridyldiylium dibromide

2,2′-Bipyridine (1.56 g, 10 mmol, Sigma-Aldrich, ≥99%) was dissolved in ethanol (50 mL, absolute, Sigma-Aldrich). To this solution, an excess of 1,2-dibromoethane (3.75 g, 20 mmol, Sigma-Aldrich, 98%) was added dropwise. The reaction mixture was refluxed at 80 °C for 18 h under stirring. After cooling to room temperature, the precipitate formed was filtered, washed with cold ethanol (3 × 5 mL), and recrystallized from ethanol/water (1:1 v/v) to afford the diium salt as a crystalline solid. The resulting product was characterized by liquid-state NMR (^{1}H and ^{13}C) and Fourier-transform infrared (FTIR) spectroscopy.

4.2.4. Synthesis of 1,1′-propylenediyl-2,2′-bipyridyldiylium dibromide

2,2′-Bipyridine (1.56 g, 10 mmol, Sigma-Aldrich (St. Louis, MO, USA), ≥99%) was dissolved in dry acetonitrile (30 mL, anhydrous, Sigma-Aldrich). To this solution, 1,3-dibromopropane (2.03 g, 10 mmol, Sigma-Aldrich, 98%) was added dropwise. The mixture was sealed in a thick-walled glass reactor and heated at 120 °C for 12 h. After cooling to room temperature, the reaction mixture was poured into excess diethyl ether (100 mL, Sigma-Aldrich, ≥99.5%), resulting in a yellow precipitate. The solid was filtered, washed with ether (3 × 10 mL), and dried under vacuum. Final purification was carried out by recrystallization from ethanol, yielding the diazepine salt as a crystalline dibromide. The resulting product was characterized by liquid-state NMR (^{1}H and ^{13}C) and Fourier-transform infrared (FTIR) spectroscopy.

4.3. Photo- and Electrochemical Characterization

4.3.1. Valence Band Energy Measurements

Valence band energy of UiO-66(Zr)-NH$_2$ and MIL-125(Ti)-NH$_2$ was determined by XPS (SPECS GmbH, Berlin, Germany), recording the photoemisson spectra of both solids and plotting the tangent to the low binding energy edge of the signal. The intersection of this tangent with the background baseline was taken as the valence band maximum (VBM) relative to the work function of the instrument. Equation (1) correspond to the calculations made in which E$_{VBM}$ corresponds to the energy of the VBM, E$_{onset}$ is the experimental energy onset of photo emitted electrons from the sample, Φ is the work function of the instrument and −4.44 eV refers to the vacuum energy level. This value can then be combined with the MOF optical band gap (from UV–Vis or diffuse reflectance) to estimate the conduction band minimum.

$$E_{VBM} = E_{onset} + \Phi + 4.44 \text{ eV} \tag{1}$$

4.3.2. Optical Bandgap Determination

The optical bandgap of MIL-125-NH$_2$ and UiO-66-NH$_2$ was determined by first recording the UV–Vis diffuse reflectance spectroscopy using a Cary 5000 Varian spectrophotometer (Agilent Technologies, Santa Clara, CA, USA) and BaSO$_4$ as white reference. Approximately 10–15 mg of finely ground dry powder was placed in the sample holder, and reflectance spectra were collected in the range of 200–800 nm. The Kubelka–Munk function (Equation (2)) was applied to convert diffuse reflectance (R_∞) into absorption values:

$$F(R_\infty) = \frac{(1 - R_\infty)^2}{2R_\infty} \tag{2}$$

The bandgap energy (E_g) was estimated using the Tauc plot. Literature typically attributes an indirect band gap to both MIL-125-NH$_2$ and UiO-66-NH$_2$. Accordingly, reflectance data were fitted according to Equation (3):

$$[F(R_\infty) \, h\nu]^{\frac{1}{2}} \, vs. \, h\nu \tag{3}$$

where *hv* is the photon energy. Extrapolation of the linear region of the plot to the energy axis provided an estimate of the band gap.

4.3.3. Conduction Band Edge Energy Minimum Determination

Conduction band energy levels were estimated from Mott–Schottky analysis. MOFs were processed into working electrodes by dispersing 50 mg of photocatalyst in a terpineol/acetone solution and drop-casting the suspension onto freshly cleaned FTO conducting glass substrates. The electrodes were dried at 150 °C overnight.

Electrochemical measurements were conducted in a three-electrode cell using the MOF-modified FTO as the working electrode, Ag/AgCl as the reference electrode, and a carbon rod as the counter electrode. A 0.1 M Na$_2$SO$_4$

aqueous solution was used as electrolyte under N_2 atmosphere. Capacitance values were recorded with a Gamry Reference 1010 potentiostat in the frequency range of 100–1000 Hz and analyzed using Gamry Echem Analyst software (Gamry Instruments, Warminster, PA, USA).

The flat band potential (E_{fb}) was determined from the intercept of the linear extrapolation of the $1/C^2$ vs. applied potential plot. This value was taken as an approximation of the conduction band edge position.

4.3.4. Cyclic Voltammetry Measurements

The redox potential of the molecules used as redox mediators was measured by cyclic voltammetry. Solutions of the redox mediators at a concentration of 0.1–0.2 M were prepared in water using 0.1 M Na_2SO_4 as the supporting electrolyte. A conventional one-compartment cell with three-electrode setup was employed, consisting of an Ag/AgCl reference electrode, a platinum working electrode, and a carbon rod counter electrode.

The applied potential range was set between –0.8 and +1.5 V, and the current response was recorded. Each cyclic voltammogram was repeated at least five times for reproducibility. Measurements were carried out in a 50 mL electrochemical cell under N_2 atmosphere using a Gamry Reference 1010 potentiostat. Data were analyzed with Gamry Echem Analyst software.

4.4. Photocatalytic Measurements

Photocatalytic suspension experiments were conducted under illumination with a custom-made white LED lamp (predominant wavelength ≈ 450 nm) powered by a DC supply (maximum voltage and current intensity of 30 V and 5 A, respectively). The LED was operated at a light intensity of 30 mW cm^{-2} as determined by a calibrated photodiode as the illuminated area was 0.5 cm^2. The irradiation area was limited Sample absorbances were recorded using a Cary 500 UV–Vis spectrophotometer. The photocatalyst was dispersed by sonication in water at a concentration of 1 mg·mL^{-1}. The organic molecule was prepared in aqueous solution at a concentration of 1.0×10^{-4} M.

Reaction setup**.** Experiments were carried out in a Hellma high-performance quartz cuvette with a total volume of 3.2 mL. The cuvette was sequentially filled with 2.5 mL of the mediator solution and 0.2 mL of the photocatalyst suspension. For electron mediators 0.5 mL of methanol was added and the cuvette was capped with a septum and purged with Ar for 5 min and further sonicated for 10 min to ensure homogeneity. For hole mediators, the cuvette was filled with additional 0.5 mL of deionized MilliQ water and the cuvette was purged with O_2 for at least 5 min. The cuvette was illuminated laterally through an opaque mask with a 0.5 cm^2 hole, placing it in front of the LED at a distance of 10 cm. Irradiations were carried out typically for a few minutes. Figure S5 provides a digital photograph of the irradiation system and its geometry.

Measurements. UV–Vis absorbance spectra were recorded between 10 s and 10 min of irradiation. The short exposure times (a few minutes) and the low light intensity ensures that no photocatalyst degradation occurs.

4.5. Light-to-Fuel Efficiency and Apparent Quantum Yield Calculations

The light-to-fuel efficiency (η) was determined by comparing the chemical energy stored in the reaction products with the incident light energy. The efficiency was calculated according to:

$$\eta\ (\%) = \frac{n \cdot \Delta G}{I_{solar}\ A \cdot t} \times 100 \tag{4}$$

where n is the number of moles of product formed, ΔG is the Gibbs free energy change per mole of product, I_{solar} is the light irradiance (W·m^{-2}), A is the illuminated area (m^2), and t is the irradiation time (s). For instance, in the case of methyl viologen, n is 9×10^{-7} mol, ΔG was 45,200 J mol^{-1}, I_{solar} is 30×10^{-3} W cm^{-2}, A was 0.5 cm^2 and t is 14 s.

The apparent quantum yield (AQY) was determined as the ratio of the number of electrons effectively transferred in the reaction to the number of incident photons, expressed as:

$$AQY\ (\%) = \frac{N_{e^-}}{N_{photon}} \times 100 \tag{5}$$

with

$$N_{photon} = \frac{P \cdot t}{E_{photon}};\ E_{photon} = \frac{hc}{\lambda};\ P = I \cdot A \tag{6}$$

where P is the optical power of the incident light (W), E_{photon} is the energy per photon at wavelength λ, h is Planck's constant, and c is the speed of light. For hydrogen evolution, $N_{e-} = $ mols $\times N_A$; ($N_A = 6.022 \times 10^{23}$ mol^{-1}). Although a polychromatic white LED was used in the photocatalytic measurements, a nominal wavelength of 450 nm was considered in the calculations. Figure S6 in supporting information provide the emission spectrum of the LED used in these measurements that was operated at a power of 10 mW cm^{-2}. As it can be seen there, LED emission has a maximum intensity emission centered at 450 nm. For the present calculations, it was considered as a valid simplification as if all the LED light intensity was emitted at 450 nm. It was considered that all the emitted photons per surface area unit were absorbed by the mediators (incident vs. absorbed photons per area unit 1).

Supplementary Materials

The additional data and information can be downloaded at: https://media.sciltp.com/articles/others/25111014 23222640/Photocatalysis-2508000310-Supplementary-Materials-FC-done.pdf. Figure S1. Diffuse reflectance spectra and corresponding Tauc plots of UiO-66(Zr)-NH$_2$ and MIL-125(Ti)-NH$_2$ photocatalysts. Figure S2. Valence band edge positions determined from the onset of photoelectron emission in XPS spectra, corrected by the instrument work function, for UiO-66(Zr)-NH$_2$ and MIL-125(Ti)-NH$_2$. Figure S3. Mott–Schottky plots from electrochemical impedance spectroscopy used to estimate the conduction band potentials of UiO-66(Zr)-NH$_2$ (working frequencies: 100 Hz, red; 500 Hz, black) and MIL-125(Ti)-NH$_2$ (working frequencies: 100 Hz, red; 150 Hz, blue; 500 Hz, violet; 1000 Hz, green). Figure S4. Optical spectra in the near-UV region showing the disappearance of the characteristic NADH absorption band at λ_{max} 340 nm upon photoxidation. Figure S5. Digital photograph showing LED, irradiation cuvette and the stirring system. Figure S6. Emission spectrum of the LED used to measure apparent quantum yields. Table S1. Literature survey of apparent quantum yields and light energy conversion into chemical energy. References [53–59] are cited in supplementary materials.

Author Contributions

L.T. and A.G.-B. performed the experimental part. Conceptualization of the work was made by A.G.-B. and H.G. The article was written with the contribution of all the authors. All authors have read and agreed to the published version of the manuscript.

Funding

Institutional Review Board Statement

Not applicable.

Informed Consent Statement

Not applicable.

Data Availability Statement

Data are available upon reasonable request from the corresponding authors.

Conflicts of Interest

The authors declare no conflict of interest.

Given the role as Editor-in-Chief, Hermenegildo Garcia had no involvement in the peer review of this paper and had no access to information regarding its peer-review process. Full responsibility for the editorial process of this paper was delegated to another editor of the journal.

Use of AI and AI-Assisted Technologies

No AI tools were utilized for this paper.

References

1. Centi, G.; Perathoner, S. Towards solar fuels from water and CO_2. *ChemSusChem* **2010**, *3*, 195–208.

2. Gust, D.; Moore, T.A.; Moore, A. Solar fuels via artificial photosynthesis. *Acc. Chem. Res.* **2009**, *42*, 1890–1898.

3. Han, H.; Li, C. Photocatalysis in solar fuel production. *Natl. Sci. Rev.* **2015**, *2*, 145–147.

4. Chen, X.; Shen, S.; Guo, L.; et al. Semiconductor-based photocatalytic hydrogen generation. *Chem. Rev.* **2010**, *110*, 6503–6570.

5. Kamat, P.V.; Bisquert, J. Solar fuels. Photocatalytic hydrogen generation. *J. Phys. Chem. C* **2013**, *117*, 14873–14875.

6. Nishiyama, H.; Yamada, T.; Nakabayashi, M.; et al. Photocatalytic solar hydrogen production from water on a 100-m^2 scale. *Nat. Rev. Mater.* **2021**, *598*, 304–307.

7. Lu, Z.; Gao, J.; Rao, S.; et al. A multifunctional membrane based on TiO_2/PCN-224 heterojunction with synergistic photocatalytic-photothermal activity under visible-light irradiation. *Appl. Catal. B Environ.* **2024**, *342*, 123374.

8. Fang, S.; Rahaman, M.; Bharti, J.; et al. Photocatalytic CO_2 reduction. *Nat. Rev. Methods Primers* **2023**, *3*, 61.

9. Khan, M.; Akmal, Z.; Tayyab, M.; et al. MOFs materials as photocatalysts for CO_2 reduction: Progress, challenges and perspectives. *Carbon Capture Sci. Technol.* **2024**, *11*, 100191. https://doi.org/10.1016/j.ccst.2024.100191.

10. Jiang, H.; Li, J.; Ren, W.; et al. Atomic-Level Engineering of Amide-bonded Ohmic-junctions for Synergistic Photocatalytic CO_2-to-CO Conversion and H_2O_2 Production via Barrier-Free Charge Transfer in Pure H_2O. *Appl. Catal. B Environ. Energy* **2025**, *378*, 125638.

11. Shen, H.; Yang, M.; Hao, L.; et al. Photocatalytic nitrogen reduction to ammonia: Insights into the role of defect engineering in photocatalysts. *Nano Res.* **2022**, *15*, 2773–2809.

12. Dhakshinamoorthy, A.; Li, Z.; Yang, S.; et al. Metal–organic framework heterojunctions for photocatalysis. *Chem. Soc. Rev.* **2024**, *53*, 3002–3035. https://doi.org/10.1039/D3CS00205E.

13. Navalón, S.; Dhakshinamoorthy, A.; Álvaro, M.; et al. Metal–Organic Frameworks as Photocatalysts for Solar-Driven Overall Water Splitting. *Chem. Rev.* **2023**, *123*, 445–490. https://doi.org/10.1021/acs.chemrev.2c00460.

14. Li, K.; Peng, B.; Peng, T. Recent advances in heterogeneous photocatalytic CO_2 conversion to solar fuels. *Acs Catal.* **2016**, *6*, 7485–7527.

15. Detz, R.; Reek, J.; Van Der Zwaan, B. The future of solar fuels: When could they become competitive? *Energy Environ. Sci.* **2018**, *11*, 1653–1669.

16. Kabir, E.; Kumar, P.; Kumar, S.; et al. Solar energy: Potential and future prospects. *Renew. Sustain. Energy Rev.* **2018**, *82*, 894–900.

17. Nayak, P.K.; Mahesh, S.; Snaith, H.J.; et al. Photovoltaic solar cell technologies: Analysing the state of the art. *Nat. Rev. Mater.* **2019**, *4*, 269–285.

18. Parida, B.; Iniyan, S.; Goic, R. A review of solar photovoltaic technologies. *Renew. Sustain. Energy Rev.* **2011**, *15*, 1625–1636.

19. Polman, A.; Knight, M.; Garnett, E.C.; et al. Photovoltaic materials: Present efficiencies and future challenges. *Science* **2016**, *352*, aad4424.

20. Yu, T.; He, W.; Zhang, Q.; et al. Advanced nanomaterials and characterization techniques for photovoltaic and photocatalysis applications. *Acc. Mater. Res.* **2023**, *4*, 507–521.

21. Chen, S.; Takata, T.; Domen, K. Particulate photocatalysts for overall water splitting. *Nat. Rev. Mater.* **2017**, *2*, 1–17.

22. Bie, C.; Wang, L.; Yu, J. Challenges for photocatalytic overall water splitting. *Chem* **2022**, *8*, 1567–1574.

23. Zhu, Z.; Liu, X.; Bao, C.; et al. How efficient could photocatalytic CO_2 reduction with H_2O into solar fuels be? *Energy Convers.* **2020**, *222*, 113236.

24. Schmidt, R. Photosensitized generation of singlet oxygen. *Photochemistryphotobiology* **2006**, *82*, 1161–1177.

25. Piguillem, S.V.; Gomez, G.E.; Tortella, G.R.; et al. Based Analytical Devices Based on Amino-MOFs (MIL-125, UiO-66, and MIL-101) as Platforms towards Fluorescence Biodetection Applications. *Chemosensors* **2024**, *12*, 208.

26. Mohamadpour, F.; Amani, A.M. Photocatalytic systems: Reactions, mechanism, and applications. *RSC Adv.* **2024**, *14*, 20609–20645.

27. Luu, C.L.; Nguyen, T.T.V.; Nguyen, T.; et al. Synthesis, characterization and adsorption ability of UiO-66-NH_2. *Adv. Nat.Sci. Nanosci. Nanotechnol.* **2015**, *6*, 025004. https://doi.org/10.1088/2043-6262/6/2/025004.

28. Kampouri, S.; Nguyen, T.N.; Spodaryk, M.; et al. Concurrent Photocatalytic Hydrogen Generation and Dye Degradation Using MIL-125-NH_2 under Visible Light Irradiation. *Adv. Funct. Mater.* **2018**, *28*, 1806368. https://doi.org/10.1002/adfm.201806368.

29. Balčiūnas, S.; Pavlovaitė, D.; Kinka, M.; et al. Dielectric Spectroscopy of Water Dynamics in Functionalized UiO-66 Metal-Organic Frameworks. *Molecules* **2020**, *25*, 1962.

30. Zhang, W.; Wang, L.; Zhang, J. Preparation of Ag/UiO-66-NH_2 and its application in photocatalytic reduction of Cr(VI) under visible light. *Res. Chem. Intermed.* **2019**, *45*, 4801–4811. https://doi.org/10.1007/s11164-019-03865-6.

31. Meng, J.; Chen, Q.; Lu, J.; et al. Z-Scheme Photocatalytic CO_2 Reduction on a Heterostructure of Oxygen-Defective ZnO/Reduced Graphene Oxide/UiO-66-NH_2 under Visible Light. *ACS Appl. Mater. Interfaces* **2019**, *11*, 550–562. https://doi.org/10.1021/acsami.8b14282.

32. Wang, M.; Yang, L.; Yuan, J.; et al. Heterostructured Bi_2S_3@NH_2-MIL-125(Ti) nanocomposite as a bifunctional photocatalyst for Cr(vi) reduction and rhodamine B degradation under visible light. *RSC Adv.* **2018**, *8*, 12459–12470. https://doi.org/10.1039/C8RA00882E.

33. Kavun, V.; Uslamin, E.; van der Linden, B.; et al. Promoting Photocatalytic Activity of NH_2-MIL-125(Ti) for H_2 Evolution Reaction through Creation of Ti^{III}- and Co^{I}-Based Proton Reduction Sites. *ACS Appl. Mater. Interfaces* **2023**, *15*, 54590–54601. https://doi.org/10.1021/acsami.3c15490.

34. Shi, X.; Lian, X.; Yang, D.; et al. Facet-engineering of NH_2-UiO-66 with enhanced photocatalytic hydrogen production performance. *Dalton Trans.* **2021**, *50*, 17953–17959. https://doi.org/10.1039/D1DT03424C.

35. Sagara, T.; Tahara, H. Redox of viologen for powering and coloring. *Chem. Rec.* **2021**, *21*, 2375–2388.

36. Daeneke, T.; Uemura, Y.; Duffy, N.W.; et al. Aqueous dye-sensitized solar cell electrolytes based on the ferricyanide-ferrocyanide redox couple. *Adv. Mater.* **2012**, *24*, 1222–1225.

37. Reyes, R.L.; Tanaka, K. The NAD^+/NADH redox couple—Insights from the perspective of electrochemical energy transformation and biomimetic Chemistry. *Kimika* **2017**, *28*, 32–43.

38. Michaelis, L.; Hill, E.S. The viologen indicators. *J. Gen. Physiol.* **1933**, *16*, 859.

39. Alvaro, M.; Carbonell, E.; Ferrer, B.; et al. Semiconductor behavior of a metal-organic framework (MOF). *Chem. A Eur. J.* **2007**, *13*, 5106–5112.

40. De Miguel, M.; Ragon, F.; Devic, T.; et al. Evidence of Photoinduced Charge Separation in the Metal–Organic Framework MIL-125 (Ti)-NH_2. *ChemPhysChem* **2012**, *13*, 3651–3654.

41. Dhakshinamoorthy, A.; Asiri, A.M.; Garcia, H. Metal–organic framework (MOF) compounds: Photocatalysts for redox reactions and solar fuel production. *Angew. Chem. Int. Ed.* **2016**, *55*, 5414–5445.

42. de Lacey, A.L.; Fernández, V.M. pH-Dependent redox behaviour of asymmetric viologens. *J. Electroanal. Chem.* **1995**, *399*, 163–167.

43. Collyer, S.D.; Davis, F.; Lucke, A.; et al. The electrochemistry of the ferri/ferrocyanide couple at a calix[4]resorcinarenetetrathiol-modified gold electrode as a study of novel electrode modifying coatings for use within electro-analytical sensors. *J. Electroanal. Chem.* **2003**, *549*, 119–127.

44. Qarah, N.A.; Basavaiah, K.; Abdulrahman, S.A. Spectrophotometric determination of ethionamide in pharmaceuticals using Folin–Ciocalteu reagent and iron(III)-ferricyanide as chromogenic agents. *J. Taibah Univ. Sci.* **2017**, *11*, 718–728.

45. Saleh, F.S.; Rahman, M.R.; Okajima, T.; et al. Determination of formal potential of NADH/NAD^+ redox couple and catalytic oxidation of NADH using poly (phenosafranin)-modified carbon electrodes. *Bioelectrochemistry* **2011**, *80*, 121–127.

46. Doménech, A.; García, H.; Doménech-Carbó, M.T.; et al. Electrochemistry of metal—organic frameworks: A description from the voltammetry of microparticles approach. *J. Phys. Chem. C* **2007**, *111*, 13701–13711.

47. Kosower, E.M.; Cotter, J.L. Stable free radicals. II. The reduction of 1-methyl-4-cyanopyridinium ion to methylviologen cation radical. *J. Am. Chem. Soc.* **1964**, *86*, 5524–5527.

48. Yamauchi, K.; Kawano, K.; Yatsuzuka, K.; et al. Viologen-Radical-Driven Hydrogen Evolution from Water Catalyzed by Co-NHC Catalysts: Radical Scavenging by Nitrate and Volmer-Heyrovsky-like CPET Pathway. *J. Am. Chem. Soc.* **2025**, *147*, 5602–5614.

49. Harriman, A.; Porter, G. Viologen/Platinum systems for hydrogen generation. *J. Chem.Soc. Faraday Trans. 2 Mol. Phys.* **1982**, *78*, 1937–1943.

50. Li, Z.; Zhang, X.; Luo, Y.; et al. An electrochemical sensor based on the composite UiO-66-NH_2/rGO for trace detection of Pb(II) and Cu(II). *Chem. Phys. Lett.* **2023**, *830*, 140825. https://doi.org/10.1016/j.cplett.2023.140825.

51. Bravo Fuchineco, D.A.; Heredia, A.C.; Mendoza, S.M.; et al. Synthesis, Characterization and Catalytic Activity of UiO-66-NH_2 in the Esterification of Levulinic Acid. *Appl. Nano* **2021**, *2*, 344–358.

52. Dan-Hardi, M.; Serre, C.; Frot, T.; et al. A New Photoactive Crystalline Highly Porous Titanium(IV) Dicarboxylate. *J. Am. Chem. Soc.* **2009**, *131*, 10857–10859. https://doi.org/10.1021/ja903726m.

53. Wang, Z.; Inoue, Y.; Hisatomi, T.; et al. Overall water splitting by Ta_3N_5 nanorod single crystals grown on the edges of $KTaO_3$ particles. *Nat. Catal.* **2018**, *1*, 756–763.

54. Wang, Q.; Nakabayashi, M.; Hisatomi, T.; et al. Oxysulfide photocatalyst for visible-light-driven overall water splitting. Nature *materials* **2019**, *18*, 827–832.

55. Zhao, Z.; Goncalves, R.V.; Barman, S.K.; et al. Electronic structure basis for enhanced overall water splitting photocatalysis with aluminum doped $SrTiO_3$ in natural sunlight. *Energy Environ. Sci.* **2019**, *12*, 1385–1395.

56. Kato, H.; Asakura, K.; Kudo, A. Highly efficient water splitting into H_2 and O_2 over lanthanum-doped $NaTaO_3$ photocatalysts with high crystallinity and surface nanostructure. *J. Am. Chem. Soc.* **2003**, *125*, 3082–3089.

57. Goto, Y.; Hisatomi, T.; Wang, Q.; et al. A particulate photocatalyst water-splitting panel for large-scale solar hydrogen generation. *Joule* **2018**, *2*, 509–520.

58. Liu, T.; Pan, Z.; Kato, K.; et al. A general interfacial-energetics-tuning strategy for enhanced artificial photosynthesis. *Nat. Commun.* **2022**, *13*, 7783.

59. Chen, D.; Chen, W.; Wu, Y.; et al. Covalent organic frameworks containing dual O_2 reduction centers for overall photosynthetic hydrogen peroxide production. *Angew. Chem. Int. Ed.* **2023**, *62*, e202217479.